Materials and Design 182 (2019) 108045

Contents lists available at ScienceDirect

Materials and Design

journal homepage: www.elsevier.com/locate/matdes

Microstructure evolution of the rapidly solidified alloy powders and composite powders

Q. Yang [a], Y.T. Liu [b], J. Liu [a], L. Wang [a], Z. Chen [a,*], M.L. Wang [c], S.Y. Zhong [c,*], Y. Wu [c], H.W. Wang [a]

[a] State Key Laboratory of Metal Matrix Composites, Shanghai Jiao Tong University, Shanghai 200240, PR China
[b] Beijing Institute of structure and environment Engineering, Beijing 100076, PR China
[c] School of Materials Science and Engineering, Shanghai Jiao Tong University, Shanghai 200240, PR China

HIGHLIGHTS

- Featureless, cellular/dendrite microstructures are formed within the alloy powders.
- The microstructure evolutions and transitions depend on the thermal history of the droplet.
- The breaking down of planar interface is discussed from critical undercooling, cooling rate and interface velocity.
- The non-planar solid/liquid interface and lower undercooling make the discrepancy of the location of nanoparticles.
- The temperature disturbance and multiple nucleation events lead to equiaxed microstructure in the composite powders.

GRAPHICAL ABSTRACT

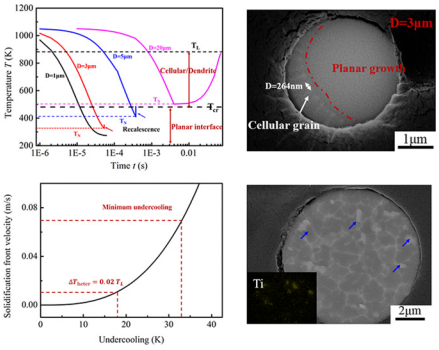

ARTICLE INFO

Article history:
Received 6 April 2019
Received in revised form 27 June 2019
Accepted 16 July 2019
Available online 17 July 2019

Keywords:
Rapid solidification
Solute trapping
Cellular/dendrite
Particles

ABSTRACT

In the present work, the size-dependent microstructure evolution of the Al-Zn-Mg-Cu alloy powders and the TiB_2/Al-Zn-Mg-Cu composite powders are studied experimentally and theoretically. Several different types of microstructures are formed within alloy powders as a function of powder size but just one type is formed within the composite powders. The transitions in microstructure within a powder such as planar interface breaking down into cellular microstructure are also observed. The occurrence of the planar interface is analyzed in terms of critical undercooling and critical cooling rate, and the breaking down of planar interface is correlated with the thermal history of the droplets modeled by Newtonian thermokinetics and interface velocity modeled by BCT models. In the composite powders, the location of TiB_2 particles depends on the entrapment/pushing by the solid/liquid interface. The disturbance of temperature field and multiple nucleation sites due to the introduction of TiB_2 particles contribute to the variation in the microstructure of alloy powders and composite powders.

1. Introduction

The metal-based additive manufacturing, or three-dimensional (3D) printing is a promising revolutionary technology applied in the field of aerospace, biomedical and automotive industries [1,2]. Therefore

* Corresponding authors.
E-mail addresses: zhe.chen@sjtu.edu.cn (Z. Chen), shengyi.zhong@sjtu.edu.cn (S.Y. Zhong).

https://doi.org/10.1016/j.matdes.2019.108045

much effort has been devoted to designing novel metal powders. It is reported that introducing nanoparticles as solidification nucleants can avoid intolerable solidification microstructure with columnar grains and periodic cracks [2]. Both the processes of 3D printing and atomization to fabricate powders are characteristic rapid solidification processes. Furthermore, novel metals powders are also the feedstock of conventional powder metallurgy routine. Therefore it is necessary to investigate the microstructure of the metal powders during atomization.

As for rapid solidification process, a large deviation from thermodynamic equilibrium leads to kinetically modified properties which do not form under conditions at equilibrium, such as extended solute solubility, structure refinement, non-equilibrium phase formation and morphology change [3–5]. According to typical strengthening mechanisms [6,7], these characteristic features obtained by rapid solidification give rise to significant strength increment by sintering these powders into designed high performance objects, especially for the age-hardening alloys such as Al-Zn-Mg-Cu, Al-Cu-Mg, and Al-Mg-Si alloys. Li et al. [8] have successfully fabricated an in-situ nano-TiB_2 decorated AlSi10Mg composite powders by atomization for selective laser melting and produced nanocomposites with the ultimate tensile strength of 530 MPa.

The gas atomization method is one of the important rapid solidification techniques and several types of primary microstructures are formed within atomized powders including eutectic, dendrite and cellular microstructure [9]. The microstructure morphology variation depends on solidification behavior. Mehrabian et al. [10] have related this morphology change with two parameters: solidification rate and temperature gradient. Trivedi et al. [11] took an inverse approach in which the measured eutectic spacing within droplets was compared with TMK model to obtain the interface velocity and interface undercooling. However, this method depending on the measured accuracy could not predict the microstructure of powders with other compositions. S. Ahn et al. [12] have modeled the thermal history of fine droplets with Newtonian thermokinetics as a function of flight distance with a series of parameters such as powder size, gas velocity, and nucleation temperature. However, the nucleation temperature as a function of droplet size is not determined. Besides, the systematic investigation on the microstructure of Al-Zn-Mg-Cu alloy powders as candidates of ultrahigh strength aluminum alloy ($\sigma_{0.2} > 800$ MPa) is rarely reported.

Currently, the Al-Zn-Mg-Cu alloys cannot be 3D printed unless the nucleants are introduced. However, the rapid solidification conditions for alloy droplets coupled with nucleants such as nanoparticles are too complicated to be characterized experimentally. Most studies focused on the grain refining effect of the particles in the castings [13–15]. And there are several papers which investigated the injection behavior of particles into droplets during co-atomization spraying process [16,17], but the role of in-situ particles on the microstructure of the atomized powders is rarely studied.

The present work was undertaken to provide further insight into morphological size-dependent microstructure evolution of the alloy powders and composite powders. These microstructure transitions are correlated with the thermal history of the droplets, especially the nucleation temperature is determined as a function of powder size. Then the microstructure of alloy powders and composite powders is to be compared. Besides, the effect of in-situ particles on the microstructure of the powders is to be discussed based on the experimental observations and theoretical calculations

2. Experimental procedure

The *Al*/TiB_2 ingots were fabricated by the typical salt-metal reaction method, details can be found in ref. [18]. The designed Al-9Zn-2.5 Mg-2.4Cu-0.1Zr (8 wt% TiB_2) alloy (composite) castings were produced by remelting Al (Al/TiB_2) ingots with pure Zn, Mg, and Al—Cu master alloy. Then the Al-Zn-Mg-Cu alloy and composites with 8 wt% TiB_2 ingots were put into the crucible and superheated to 780 °C holding for 30 min. The ingots were totally melted. The melt was delivered into the atomizer and broken down into fine droplets under the impact of rapid moving N_2 gas. Finally, the alloy powders and composite powders were obtained by cooling down of the droplets.

The microstructures of the powders were characterized by TESCAN MAIA3 scanning electron microscope under the backscattered electron (BSE) mode. The powders were mounted in mounting resin epoxy and then polished with increasingly finer emery paper. After a final emery paper polishing with 5 μm diamond powder, the powders were then polished with 5, 1.5 and 0.5 μm colloidal diamond solution followed by 0.05 μm colloidal silica solution and then subjected to metal spraying for the purpose of good conductivity. The electron backscattered diffraction (EBSD) of the powder was carried out on the TESCAN MAIA3 equipped with BRUKER e-Flash^{HR} electron backscatter diffraction (EBSD) detector. The sample was fabricated by FIB-SEM instrument TESCAN LYRA3 XM. The transmission electron microscopy (TEM) observation was conducted on Talos F200X equipped with scanning transmission electron microscopy (STEM) detector operated at 200 kV. The TEM specimens were fabricated by section using FIB-SEM instrument TESCAN LYRA3 XM.

3. Results

3.1. The microstructure of the alloy powders

Fig. 1a shows the cross-section microstructure of an alloy powder with a diameter of 48 μm. The grain boundaries are in lighter contrast in backscattered electron images (BSE) mode. The powder exhibits equiaxed microstructure morphology and the average grain size is about 1 μm. Fig. 1b gives the scanning transmission electron micrographs (STEM) of the alloy powders, and the according EDS mappings of *Al* element and solute elements are also shown in Fig. 1c. It is revealed the interphases are formed at the grain boundaries. The solute atoms pushed by solid/liquid interface into grain boundaries during solidification give rises to the formation of the interphases. Fig. 1d displays the microstructure of a powder with a diameter of 42 μm, which is completely different from the microstructure shown in Fig. 1a. In this powder, the dendrite structure sweeps across the whole powder originating from nucleation site E as marked in the red box. Fig. 1e exhibits the BSE image with higher magnification of location E in Fig. 1d. The microstructure at the nucleation site area exhibits equiaxed morphology. The average grain size is about 1 μm. Fig. 1f gives the BSE image with higher magnification of location F as marked in the blue box in Fig. 1d. The cellular/dendrite microstructure grows outwards from the nucleation site. The secondary dendrite spacing is similar to the grain size at the nucleation site.

Fig. 2 shows the cross-section microstructures of the powders with different diameters ranging from 1.8 μm to 7 μm. In Fig. 2a single nucleation site is observed in the powder with a size of 7 μm as marked in the red arrow. The cellular morphology originates from nucleation site and spans partially across over the powder. The transition from cellular to equiaxed microstructure occurs at the opposite direction of the nucleation site. Note that the cellular spacing increases at a larger distance away from the nucleation site due to the latent heat release during solidification. Fig. 2b shows the microstructure of the powder with a diameter of 3 μm and two microstructural zones are observed. The droplet begins to solidify with a planar solid/liquid (S/L) interface. The solute trapping phenomenon occurs and the supersaturated solid solution with extended solubility is formed under the rapid moving interface. After partial solidification, the interface temperature rises due to recalescence, and then the planar interface becomes unstable and breaks down into the cellular morphology. The red dashed line indicates the location of the breaking down of the planar interface. Note that the cellular spacing is narrower at the lateral side of the powder due to the cooling effect from the surface. Fig. 2c gives another image of the microstructure of the powder with a diameter of 3 μm. The microstructure is similar to that observed in Fig. 2b, whereas the volume fraction of the

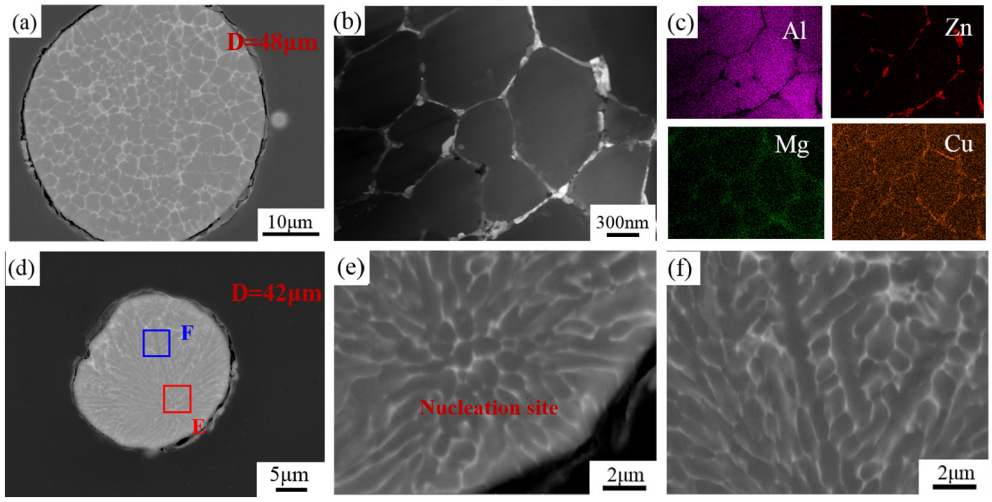

Fig. 1. (a) The cross-section microstructure of the alloy powder in backscattered electron (BSE) mode; (b) the STEM image of the alloy powder; (c) the EDS mappings of *Al* elements and solute elements; (d) the microstructure of another powder with diameter of 42 μm showing the microstructure of dendrite grains; (e) and (f) the local area marked in (d) with larger magnification.

cellular microstructure in this powder is lower than that shown in Fig. 2b. Detailed description of the growth model is provided in Fig. S1 in the supplementary materials. With further decreasing powder size to 1.8 μm, the cellular microstructure is not formed as shown in Fig. 2d. In this powder, the planar interface moves across the whole powder.

There is only one nucleation site observed in the above images. In general, the nucleation site is located at the outer surface of the powders due to severer heat convection. Multiple nucleation events can also occur due to the presence of impurities. Fig. 3 gives the cross-section microstructures of the powders with multiple nucleation sites. Fig. 3a shows the microstructure of the powder with a diameter of 40 μm and four nucleation sites are observed within the powder as marked in red dotted lines. All of these nucleation sites are located within the powder. The cellular/dendrite microstructure is observed at each nucleation site and grows outwards. The transition from cellular/dendrite structure to equiaxed structure occurs when the cellular/dendrite microstructure approaches to each other. As shown in Fig. 3b, there are three nucleation sites observed in the powder with a diameter of 30 μm. One of the nucleation sites is located at the outer surface of the powder and the rest are located within the powder. The microstructure is similar to that in Fig. 3b. However, the volume fraction of cellular/dendrite microstructure is higher. With further decreasing powder size to 12 μm, there are two nucleation sites located at the opposite side on the outer surface of the powder. The cellular grain structure originates from the nucleation site until impinging at the middle of the powder and then transforms into the equiaxed microstructure. The volume fraction of the cellular grain structure further increases. The illustration of the growth model in the droplet is provided in Fig. S2 in the supplementary materials.

Fig. 4 shows the electron back-scatter diffraction (EBSD) pattern of the cross-section of the powder with 25 μm. As it is shown in the EBSD quality in Fig. 4a, there are some grains with small angle grain boundaries (SAGBs), typically labeled as grain 1, 2 and 3. Additionally,

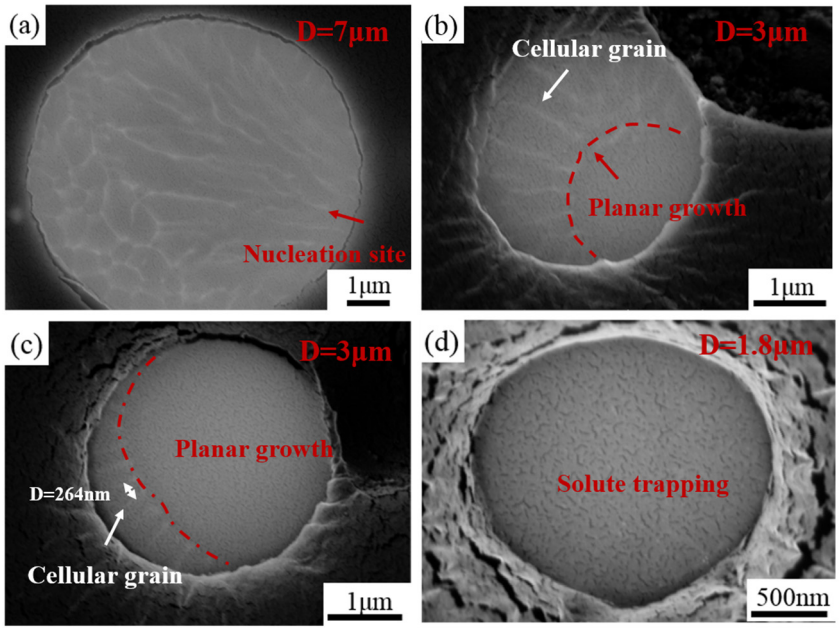

Fig. 2. The cross-section microstructures of the alloy powders with different size.

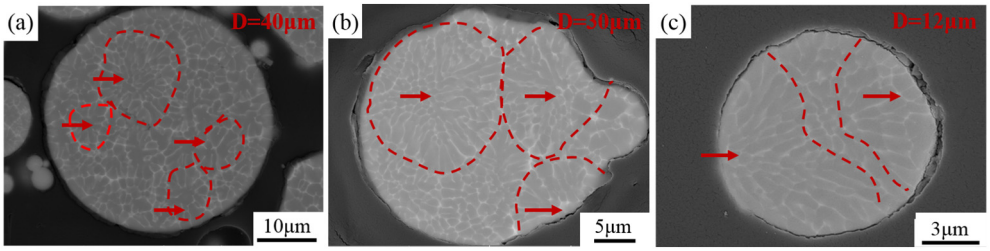

Fig. 3. The cross-section microstructures of the alloy powder with several nucleation sites.

there are more grains without SAGBs, typically labeled as grain 4, 5, 6 and 7. The different colour between the subgrains in Fig. 4b indicates a small change in the subgrains orientation. These subgrains are assumed as cellular microstructure. And the grains without SAGBs are assumed as equiaxed grains. The EDS mappings of Zn, Mg and Cu elements in Fig. 4c shows the elements segregation at the large angle grain boundaries and small grain angle grain boundaries. In this powder, the multiple nucleation events occur. And the fraction of cellular microstructure is small.

From the above analysis, the microstructures of the powders are greatly affected by powder size. The solute trapping behavior occurs in the finest powder and the supersaturated solid solution forms. With the increase of powder size, the planar solid/liquid interface breaks down into cellular microstructure and the volume fraction of cellular microstructure is inversely proportional to the powder size. With further increasing powder size, the cellular/dendrite microstructure grows across the whole powder. The equiaxed microstructure is formed in larger powders. Additionally, the number of nucleation sites also influences the solidification behavior of the atomized droplets. When there is only one nucleation site, the dendrite structure sweeps across the whole powder (Fig. 1d). However, when there are multiple nucleation sites, the cell structure grows outwards from the respective nucleation site. The equiaxed structure can be seen between the two cellular microstructure. With the decrease of powder size, most bulk heterogeneous nucleation sites such as impurities are removed and the probability of multiple nucleation is lower.

Fig. 5a shows the microstructure of the alloy powder with a diameter of 30 μm. The cross section is maybe perpendicular to the cellular growth direction or multiple nucleation events occur and only a small fraction of dendrite/cellular structure is observed. Fig. 5b gives the image of the microstructure with higher magnification. It is observed that there are interphases formed around the nucleation site which is resulted from remelting of the solidified solid due to temperature arise during recalescence. Fig. 4c displays the High Angle Annular Dark Field (HAADF) image which also shows the formation of the interphases. There are two different types of interphases observed from the Z contrast. The interphase in darker contrast is mainly composed of Cu

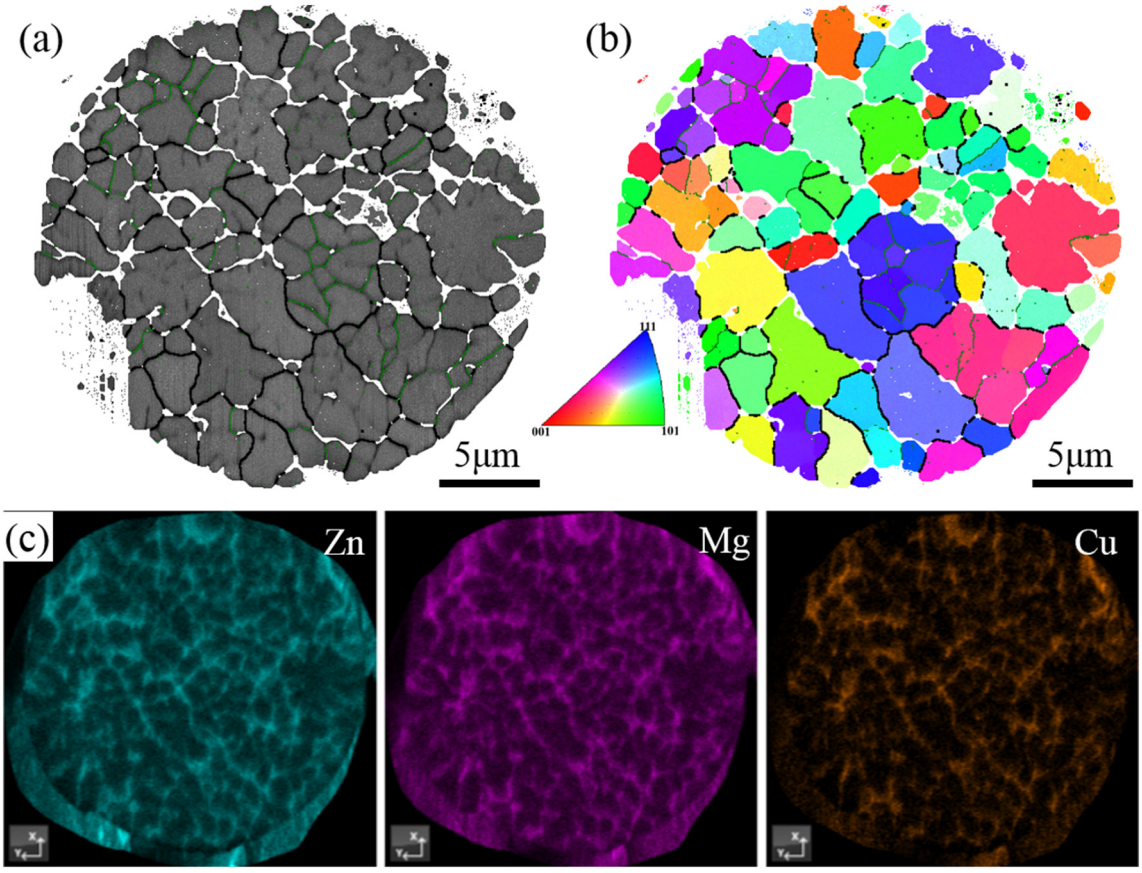

Fig. 4. (a) The electron backscattered diffraction (EBSD) pattern of the cross-section of the powder, large angle grain boundaries ($\theta > 15°$) are in thick black lines and small angle grain boundaries ($2° < \theta < 15°$) are in thin green lines; (b) the inverse pole figure (IPF) pattern; (c) the EDS mappings of Zn, Mg and Cu elements. (For interpretation of the references to colour in this figure legend, the reader is referred to the web version of this article.)

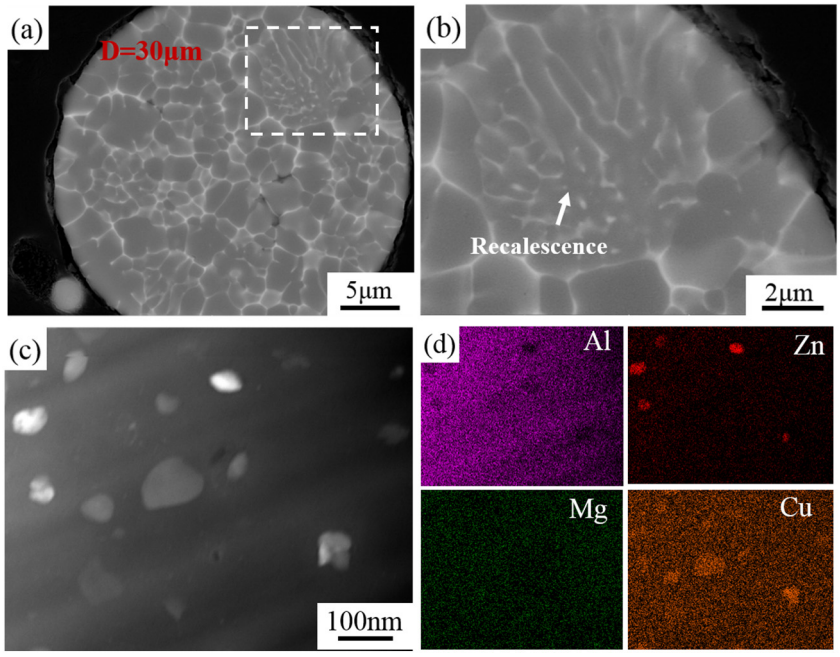

Fig. 5. (a) The microstructure of the alloy powder showing the recalescence in the local region; (b) the local region with larger magnification; (c) the STEM image of the alloy powder showing the existence of the interphases; (d) the EDS mappings of the *Al* elements and solute elements.

elements and the brighter interphase is mainly composed of Zn elements as shown by EDS mappings in Fig. 5d.

3.2. The microstructure of the composite powders

Fig. 6a shows the cross-section microstructure of the composite powders with a size of 10 μm in BSE mode and the EDS mapping of Ti elements is given in the inset. The TiB_2 particles are uniformly distributed in the aluminum alloy matrix. Only submicron TiB_2 particles are observed at this magnification due to limited resolution. Fig. 6b gives the microstructure with higher magnification. The TiB_2 particles are distributed either at the grain boundaries as pointed by blue arrows (Fig. 6a) or located within grains as pointed out by red arrows (Fig. 6b). The composite powders exhibit the equiaxed microstructure independent on the powder size, and the cellular microstructure is not observed. The cross-section microstructure of the composite powder with a diameter of 3.6 μm is shown in Fig. 6c. At the middle of the powder is located the TiB_2 particle as indicated by the blue arrow. The solute trapping occurs near the TiB_2 particle. At the outer surface of the powder, the planar S/L interface destabilizes. Fig. 5d shows the comparison of the grain size between the alloy powders and composite powders as a function of powder size. Only the equiaxed grains are measured. For larger alloy powders with a specific size, the equiaxed grains are often observed and the two hundred grains are measured. For smaller

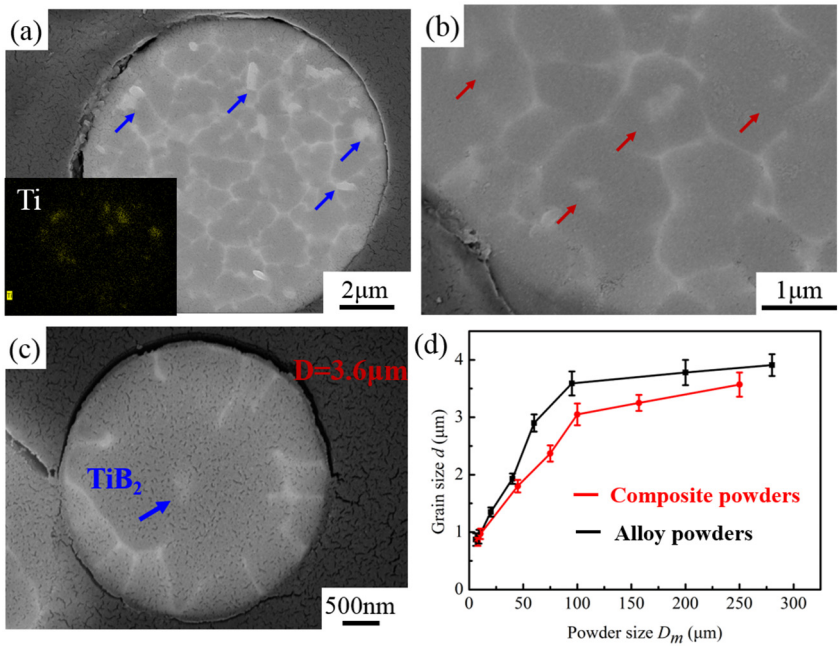

Fig. 6. (a) The cross-section microstructure of the composite powder, and the EDS mapping of Ti elements is given in the inset; (b) the microstructure of the composite powder with larger magnification; (c) the microstructure of the composite powder with diameter of 3.6 μm; (d) grain size vs. powder size.

alloy powders, the equiaxed grains exist due to multiple nucleation events and one hundred grains are measured by the software of ImageJ. For the composite powders, two hundred grains are measured for a specific powder size. Generally, the grain size of the composite powders is smaller than that of the alloy powders.

4. Discussion

4.1. Thermal history of the droplet with specified nucleation temperature

In order to analyze the size-dependent microstructure evolution of the droplets during the gas atomization process, it is necessary to model the droplet solidification process as a function of time and provide droplet thermal history understanding. In the present study, the Newtonian thermokinetic mathematical model coupled with classical nucleation theory and the specific solidification process is adopted [12,19], which neglects the temperature gradient.

During the gas atomization process, the parameter of heat transfer coefficient h describes the severe heat remove by gas media. The parameter h is influenced by cooling condition and can be estimated as the following expression:

$$\mathrm{h} = \frac{k_g}{D}\left(2 + 0.6\sqrt{Re}\sqrt[3]{Pr}\right) \tag{1}$$

where

$$\mathrm{Re} = \frac{\rho_g D|u_d - u_g|}{u_g} \tag{2}$$

$$\mathrm{Pr} = \frac{C_{pg}u_g}{k_g} \tag{3}$$

where Kg is the gas thermal conductivity, D is the diameter of the droplet, ρ_g is the density of the gas, u_d is the velocity of the droplet, u_g is the velocity of the gas, C_{pg} is the gas specific heat. Due to the variation of the velocity of the droplet and gas, the heat transfer is variable during the whole flight time. It is necessary to model the velocity history of the droplet. According to the analysis of the force including gravity force and drag force acting on the droplet, the velocity of the droplet can be estimated as following expression [20]:

$$\rho_d V_d \frac{du_d}{dt} = V_d\left(\rho_d - \rho_g\right)g + \frac{1}{2}\rho_g A_d C_D|u_g - u_d|(u_g - u_d) \tag{4}$$

where V_d, A_d, ρ_d is the volume, cross-section area and density of the droplet respectively. And

$$C_D = 0.28 + \frac{6}{\sqrt{Re}} + \frac{21}{Re} \tag{5}$$

In some papers, the change in gas velocity as a function of time is neglected. In fact, the gas velocity is variable during the whole process. Different types of gas velocity decay formulations are proposed [21]. In this study, the following expression is adopted:

$$\mathrm{u}^2 = \frac{\lambda u_0}{2t + C} \tag{6}$$

where $\mathrm{C} = -\lambda/u_0$, μ_0 is the initial gas velocity at the exit, $\lambda = \alpha\sqrt{A}$, α is the constant as 7.414 for turbulent free jet [12], A is the exit area of the orifice.

Thus the predicted variation of the droplet and gas velocity with time is numerically estimated and plotted in Fig. 7a for droplets with three typical size 1 μm, 20 μm and 100 μm. The modeling parameters are listed in Table 1 [5,12,16,22–26]. The variation of gas velocity is independent on droplet size and decays significantly. The droplet velocity increases significantly until equaling to gas velocity and then decays extensively. The maximum droplet velocity increases with decreasing droplet size and the final droplet velocity increases with increasing droplet size. Thus the heat transfer coefficient of the droplets with different size is estimated by Eq. (1) and plotted in Fig. 7b. The heat transfer coefficient tends to be constant at the final stage. The droplet size greatly inversely affects the value of heat transfer coefficient h.

The droplet in flight is supposed to undergo the different thermal process, including liquid phase cooling, nucleation and recalescence, segregated solidification, eutectic solidification, solid phase cooling. The thermal history of an undercooled droplet with size D can be described by a simple Newtonian heat transfer formulation:

$$C_{pd}\frac{dT_d}{dt} = \Delta H_d\frac{df_s}{dt} - \frac{6h}{D\rho_d}\left(T_d - T_g\right) \tag{7}$$

where

$$C_{pd} = C_L - (C_L - C_S)f_s$$

$$\Delta H_d = \Delta H_f - (C_L - C_S)f_s$$

where C_L and C_S is the specific heat of the liquid and solid respectively, f_s is the volume fraction of the solid in the droplet and T_g is the temperature of the gas, which is assumed invariable. During the liquid cooling stage, the temperature is higher than nucleation temperature and the solid has not been nucleated, thus the f_s equals to zero. The differential equation could be expressed as:

$$C_L\frac{dT_d}{dt} = -\frac{6h}{D\rho_d}\left(T_d - T_g\right) \tag{8}$$

When the droplets cool down to nucleation temperature, the droplets start to nucleate and the temperature rises significantly because recalescence takes place once solid phase has been nucleated. The volume fraction of the solid is given by the following expression:

$$f_s = \frac{3}{2}\left(\frac{x}{D}\right)^2 - \frac{1}{2}\left(\frac{x}{D}\right)^3 \tag{9}$$

where x is the distance solidified along the growth axis. The solid growth rate from droplet could be approximated as a linear function of the undercooling:

$$\frac{dx}{dt} = K_i(T_L - T_d) \tag{10}$$

where the liquid-solid interface mobility taken as 0.02 m/ s K^{-1} in the present study [12]. The maximum recalescence temperature ($\mathrm{T_R}$) is estimated when the latent heat release is equal to external heat removal rate. After recalescence, further solidification of the droplet would continue to take place according to Schiel equation. The volume fraction of the solid could be estimated as:

$$f_S = 1 - (1 - f_R)\left(\frac{T_M - T_R}{T_M - T_d}\right)^{\frac{1}{1-k_0}} \tag{11}$$

where T_M is the melting temperature which is assumed to equal to liquidus temperature. After the droplet is completely solidified, the f_s equals to 1, then the cooling rate is given as:

$$C_s\frac{dT_d}{dt} = -\frac{6h}{D\rho_d}\left(T_d - T_g\right) \tag{12}$$

The thermal cooling history is plotted in Fig. 7c and the solid fraction of the droplet as a function of flight time is plotted in Fig. 7d for droplets with diameter 1 μm, 20 μm and 100 μm which assumes that the nucleation temperature is 860 K with a small undercooling approximately

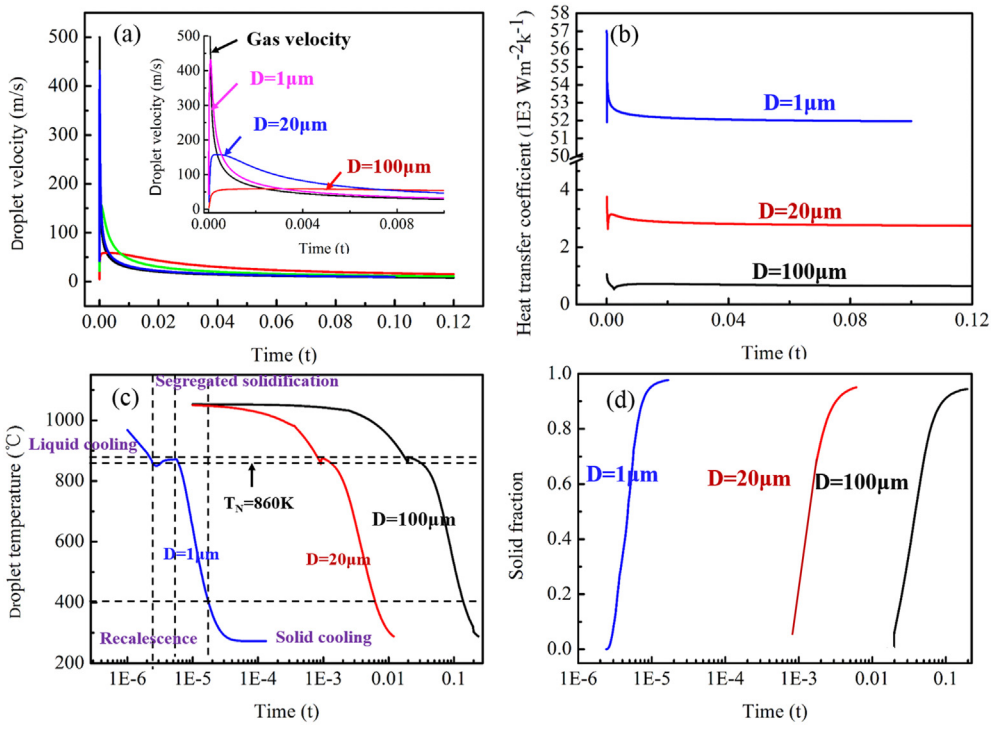

Fig. 7. (a) (b) (c) (d) The predicted drop velocity, heat transfer coefficient, droplet temperature, solid fraction variation with time assuming the nucleation temperature is 860 K.

20 K of different size. It can be clearly seen that the smaller droplets have a larger cooling rate in all solidification stages and the maximum cooling rate occurring at the liquid cooling rate is inversely proportional to the droplet size. For droplets with a size of 1 μm, the temperature of the droplets is still decreasing after reaching to nucleation temperature. It indicates that the heat release by partial solidification is lower than the heat extraction by residual liquid cooling. Nevertheless, for larger droplets, the droplet temperature instantaneously increases to the range of solidification temperature (T_L-T_S) once nucleation occurs. Furthermore, the finer droplets fully solidify within a shorter time. As it was calculated, that a 1 μm size droplet completely solidifies within the time of 1.38×10^{-5} s, whereas a 20 μm and 100 μm size droplet fully solidify within the time of 5.2×10^{-5} s and 0.179 s respectively.

Table 1
Modeling parameters.

Parameters	Physical means	Value	Units	Ref.
A_0	Exit area of the orifice	20	mm^2	Present work
ρ_d	Density of droplet	2700	Kg/m^3	[5]
ρ_g	Density of nitrogen gas	1.16	Kg/m^3	[12]
C_{pg}	Gas specific heat	1039	J/(Kg K)	[12]
K_g	Gas thermal conductivity	0.0258	W/(m K)	[12]
C_L	Liquid specific heat	1100	J/(Kg.K)	[22]
C_S	Solid specific heat	860	J/(Kg K)	[22]
ΔH_f	Latent heat of melt of droplet	$3.4 \times 1e^5$	J/Kg	[12]
T_L	Liquidus temperature	879	K	[22]
T_S	Solidus temperature	814	K	[22]
K_0	Equilibrium partion coefficient	0.143	–	[23]
α	Droplet thermal diffusion coefficient	$3.4 \times 1e^{-5}$	m^2/s	[25]
Γ	Gibbs-Thompson coefficient	$1.16 \times 1e^{-7}$	m K	[24]
σ	Interfacial energy	0.122	J/m^2	[16]
m	Liquidus slope	−5.55	K	[23]
V_d	Atom diffusion velocity	10	m/s	[22]
μ	Kinetic growth coefficient	0.3	–	[26]

4.2. The nucleation temperature and critical condition for homogeneous nucleation

In the above analysis, the size-dependent nucleation temperature is not obtained. Therefore, the thermal history of the droplets is analyzed by assuming a specific nucleation temperature. It is only reasonable when multiple nucleation occurs during solidification, especially for the existence of impurities or nucleants. It is well-acknowledged that undercooling required for heterogeneous nucleation is much lower than that for homogeneous nucleation. Thus the nucleation is difficult to be suppressed until large undercooling due to the presence of potent catalytic sites. The larger droplets increase the probability of multiple nucleation.

As for ideal single nucleation event, in fact, the nucleation of finer droplets is easier to be suppressed until larger undercooling. Zhai et al. [27] deduced a relationship between the degree of undercooling and droplet size as following expression employing classic nucleation theory:

$$\frac{\psi}{(T_L-\Delta T)\Delta T^2} = \ln\left(\frac{\frac{\pi}{6}K_V\rho_d C_L T_N^2}{6h\psi(2T_L-3\Delta T)(T_L-T_g-\Delta T)}D^4\right) \quad (13)$$

where $\psi = \frac{16\pi\sigma_{SL}^3 T_L^2}{3k_B\rho_d^2\Delta Hf^2}$, where σ_{SL} is the interfacial energy between solid and liquid, T_L is the liquidus temperature, k_B is the Boltzmann constant and K_v is the kenetic parameter. In the above equation, it is hard to obtain the explicit relation between droplet size and heat transfer coefficient. Therefore, taking the heat transfer coefficient as constant for all droplet size in the above equation would lead to error result. For droplet size with 1, 20 and 100 μm, the heat transfer coefficient is obtained according to the above Eq.(1) due to small fluctuation during the stage of solidification. Taking all parameters into the Eq.(1), the undercooling could be numerically solved as 605, 377 and 321 K, respectively.

Hirth [28] has noted that if the undercooling is high enough, solidification could take place without the interface temperature ever reaching

the solidus temperature. The critical undercooling could be estimated as following expression:

$$\overline{C}_p(\Delta T + (T_S - T_L)) \geq \Delta H \tag{14}$$

It means that heat removal during atomization is larger than latent heat release. In this alloy system, the critical undercooling is approximated as 392 K. The undercooling for droplets with a diameter of 1 μm is higher than critical undercooling for homogeneous nucleation, while the undercooling of droplets with a diameter of 20 and 100 μm is lower. Therefore, the droplet with a diameter of 1 μm would nucleate homogeneously followed by partitionless solidification in the planar interface and exhibit featureless microstructure without cells or dendrites as it is observed in the experiment.

In addition to critical undercooling criteria, S. Hariprasad et al. [29] developed the critical cooling rate theory for homogeneous nucleation as following expression:

$$\Delta T_c^2 = -A\frac{16\pi\sigma_m^3 v^2 T_L^2}{3kT_n\Delta H_f^2 \ln\left(Bd^3 10^{-3}\left(\frac{2\sigma_m T_L v}{\Delta H_f a \Delta T_c}\right)^2\left(\frac{a}{v}\right)D\left(\frac{\Delta T_c}{T^*}\right)\right)} \tag{15}$$

where A, B is the pre-exponential factor which is proposed by Hirth for consistency between experiment results and predictions. Taking ΔT_c as 392 K into the above equation, the critical cooling rate under homogeneous nucleation condition for a droplet with size 1, 20, 100 μm is 1.6×10^7, 4.7×10^9, 3.2×10^{12} K/s, respectively. The maximum cooling rate of the droplet is estimated as liquid cooing rate as 7.5×10^7, 2.9×10^6, 1.7×10^5 K/s, respectively. From the above analysis, only the cooling rate of the droplet with a diameter of 1 μm could reach the critical cooling rate for homogeneous nucleation.

In addition to full featureless microstructure free of microsegregation in the powders with the size of 1 μm, some powders with size larger than 1 μm have a mixed microstructure with two zones (Fig. 2b and c). A smooth solid/liquid interface moves partially and quickly across the droplet with extended solubility at the initial nucleation site and then breaks down to solidify with much slower rate to produce cellular microstructure. It means that at the initial stage of solidification, the critical undercooling and critical cooling rate are satisfied for homogeneous nucleation. With proceeding solidification, the droplet temperature increases and the cooling rate decreases. Then the planar solid/liquid interface is destabilized. The variation in the cooling rate and initial undercooling gives rise to significant solidification microstructure change. With decreasing the cooling rate, the solidification microstructure changes from planar through cellular to dendrite and finally to planar microstructure again. These microstructure differences and transitions were also reported in Al-Fe-V-Si [24,30] and Al—Ti [31]. The condition of transition from one growth rate regime to another regime has been discussed in ref. [32]

Fig. 8a shows the thermal history of the droplet with a size of 1, 3, 5, 20 μm and the nucleation temperature is estimated by Eq. (13). The thick black horizontal dotted line represents the critical temperature for homogeneous nucleation. It is observed that the temperature of the droplet with a size of 1 μm does not increase even during the solidification process as a result of severe heat extraction. The temperature of the droplet with a size of 3 μm increases not much during the recalescence stage as pointed by the red arrow but never reaches critical temperature for homogeneous nucleation. Therefore, it is predicted that the droplet with a size of 3 μm solidifies with the planar interface across the whole powder. As for the droplet with a size of 5 μm, the initial undercooling is satisfied for homogeneous nucleation. With further solidification, the temperature increases and reaches to above the critical temperature. Then the planar solid/liquid interface will destabilize to produce cellular microstructure. For the droplet with 20 μm, the initial undercooling is not satisfied and the solute trapping will never occur. The droplets will solidify to produce coarse cellular/dendrite microstructure. The temperature ranges for different solidification microstructure are identified. Fig. 8b shows the schematic overview of the solidification process during atomization and the single nucleation site is assumed at the outer surface of the droplet. The growth direction is along the indicated axis. Fig. 8c~e shows the illustration of the temperature and solid volume fraction evolution within droplet with a size of 1, 3 and 5 μm. The black curve lines represent the solid/liquid interface.

In the above analysis, the Newtonian heat transfer formulation combined with classic nucleation theory is used. The thermal history of the droplet is numerically analyzed. R. Mehrabian et al. [25,33] have tried to describe the thermal history of powder solidification by an enthalpy-temperature diagram which is not discussed here. The Newtonian numerical model assumes no temperature difference inside the droplet and to preserve original axisymmetric growth along the axis. Although it is often supposed reasonably for the case of gas atomization due to small Biot number equating to hr/k_L, it is found some discrepancy in the experiment. For example, it is predicted that the cellular microstructure would not form in the droplet with a size of 3 μm whereas it is found in the experiment. In fact, the temperature gradient often develops inside the droplet during solidification. The comparison of the Newtonian and non-Newtonian model found that there is little temperature difference within droplets with a size of 1 μm during the whole solidification process. As droplet size increases, the temperature gradient

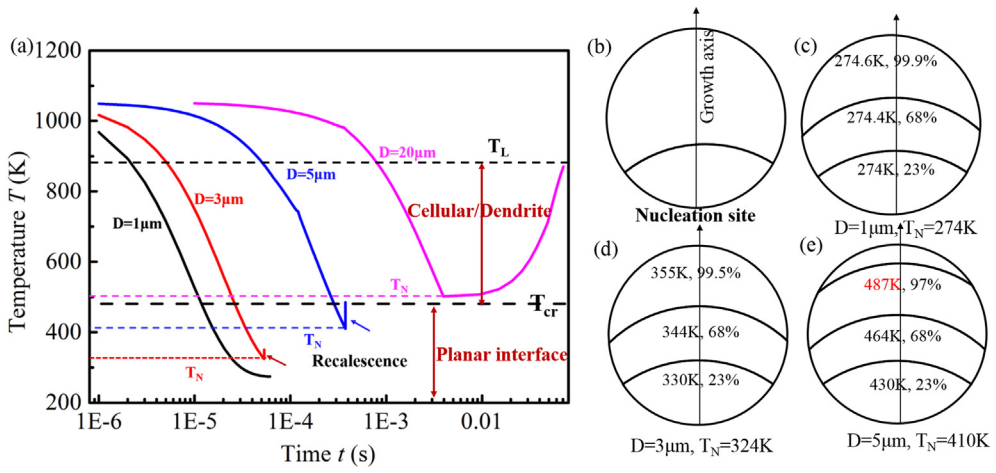

Fig. 8. (a) The droplet thermal history with different size (the nucleation temperature is calculated by Eq.(13); (b) ~ (e) illustration of the solidification of droplets with different size, the lines in the droplet are the isothermal lines, the temperature and volume fraction of solidified solid are indicated.

develops inside the droplets which is predicted by non-Newtonian model and the isothermal model is not applicable. Therefore, it is not reasonable to equal the volume temperature to interface temperature and equal volume undercooling to interface undercooling. Generally, the interface temperature is higher than the volume temperature.

4.3. Interface velocity

The occurrence of featureless microstructure without solute microsegregation could also be discussed in view of rapid moving solid/liquid interface velocity. The solute elements are usually rejected to the interface front. However, when the interface velocity is significantly greater than the solute diffusivity in the droplet, the solute atoms will be engulfed by the solid/liquid interface and solute trapping occurs. Usually, the interface velocity can be evaluated by comparing the measured cellular spacing with predicted one by the theoretical model. Lipton, Kurz and Trivedi developed a model (LKT) to predict the steady-state tip velocity under a certain total undercooling which was composed of thermal undercooling, solute undercooling and curvature undercooling [34]. Kurz, Giovanola and Trivedi [35] developed the LKT model which modified the dependence of the partition coefficient on the interface velocity. Boetting, Coriell and Trivedi extended the KGT model to include kinetics undercooling [36]. Villaret et al. [37] have successfully predicted the columnar-to-equiaxed transition in welding of a Cr—Mo ferritic stainless steel by the BCT model. Brochu et al. [38,39] have analyzed the solute trapping behavior under rapid interface velocity which is predicted by KGT model during the process of electrospark deposition. The theory of BCT model is briefly described as follows:

$$\Delta T = \Delta T_T + \Delta T_R + \Delta T_C + \Delta T_K \tag{16}$$

The first term ΔT_T is the thermal undercooling, the second term ΔT_R is the curvature undercooling, the third term ΔT_C is the solutal undercooling, the forth term ΔT_K is the kinetic undercooling. The detail expression of undercooling is given as follows:

$$\Delta T_T = \frac{\Delta H_m}{C_P} Iv(P_T) \tag{17}$$

$$\Delta T_R = 2\frac{\Gamma}{R} \tag{18}$$

$$\Delta T_C = m_L C_0 \left[1 - \frac{m_v}{m_L[1-(1-k)Iv(P_C)]}\right] \tag{19}$$

$$\Delta T_K = \frac{V}{\mu} \tag{20}$$

where ΔH_m is the heat fusion, C_P is the droplet heat capacity, $Iv(P_T)$ is the Ivantsov function of the thermal Peclet number equating to $P_T e^{P_T} E_1(P_T)$, $E_1(P_T)$ is the exponential intergral function, P_T equals to $\frac{VR}{2\alpha}$, Γ is the Gibbs-Thomson coefficient which equals to $\sigma/\Delta S_f$, σ is the interfacial energy, ΔS_f is the fusion entropy, m_L is the liquidus slope which can be determined from the equilibrium phase diagram, C_0 is the melt solute concentration, k and m_v is the partition coefficient and corrected liquidus slope respectively both of which depend on the interface velocity as follows:

$$m_v = m_L \frac{1 + k_e - k\left(1 - \ln\frac{k}{k_e}\right)}{1-k_e} \tag{21}$$

$$k = \frac{k_e + \frac{V}{V_d}}{1 + \frac{V}{V_d}} \tag{22}$$

where k_e is the equilibrium partition coefficient, V_d is the atomic diffusive speed which equals to D_0/a_0, D_0 is the solute diffusivity, a_0 is the

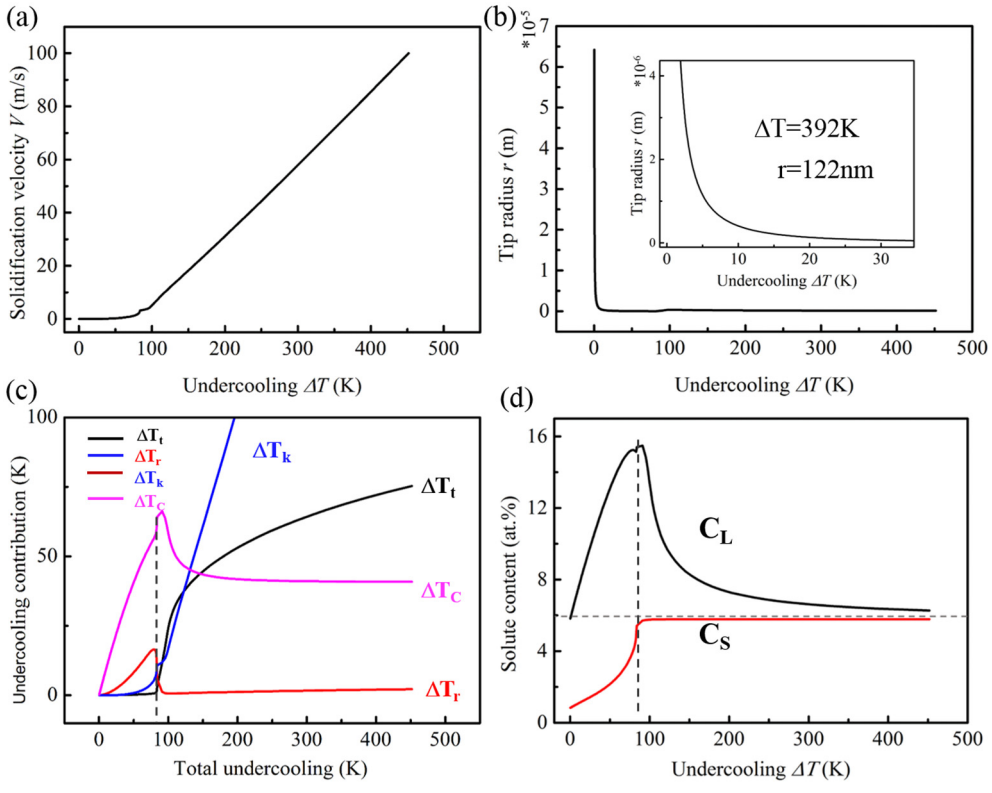

Fig. 9. (a) (b) (c) (d) Solidification velocity, tip radius, undercooling contribution and solute content as a function of the total undercooling.

atom spacing, P_C is the solutal Pelect number, μ is the kinetic growth coefficient. According to the above analysis, the total undercooling is a function of tip radius R and interface velocity V. Another equation is to relate the tip radius with interface velocity. Mullins and Sekerka [40] developed a stability equation which considered the tip radius to the shortest wavelength under local growth condition. Trivedi and Kurz [41] extended the Mullins-Sekerka stability equation to rapid solidification.

$$R = \frac{1}{\sigma^*(G_C\xi_C - G\xi_t)} \tag{23}$$

where $\sigma^*$is the stability parameter chosen as $1/(4\pi^2)$, G_C is the solute gradient is the liquid, G is the mean temperature gradient at the tip. Generally, the temperature gradient in the solid is neglected and only gradient temperature in the liquid is considered. The G_L and G_C are expressed as follows:

$$G_L = -\frac{V\Delta H_m}{\alpha C_P} \tag{24}$$

$$G_C = -\frac{VC_0(1-k)}{D_0(1-(1-k)Iv(P_C))} \tag{25}$$

The parameters ξ_C, ξ_t are given as follows:

$$\xi_t = 1 - \frac{1}{\sqrt{1+\frac{1}{\sigma^* P_T^2}}} \tag{26}$$

$$\xi_C = 1 + \frac{2k}{1-2k-\sqrt{1+\frac{1}{\sigma^* P_C^2}}} \tag{27}$$

According to the above analysis, the tip radius and interface velocity under a certain undercooling are numerically solved.

The modeling results are shown in Fig. 9. Fig. 9a shows the predicted relationship between interface undercooling and interface velocity. It is observed that the interface velocity increases significantly with increasing total interface undercooling. Fig. 9b displays the predicted relationship between the tip radius and interface undercooling. The tip radius greatly decreases with increasing total undercooling. When the total undercooling is about 392 K, the tip radius is calculated as 122 nm which is similar to the half cellular spacing measured as 132 nm (Fig. 2c). Fig. 9c exhibits the contribution of different undercooling to total undercooling. For small total undercooling, the solutal undercooling contributes significantly to total undercooling. For large total undercooling, the thermal undercooling and kinetic undercooling contributes much to total undercooling. Fig. 9d shows the relationship between liquid solute content and solid solute content with total undercooling. It is observed that with increasing total undercooling to 392 K, both the liquid solute content and solid solute content approaches to the melt composition C_0, and solidification front velocity is calculated as 82 m/s which is faster than the solute atom diffusivity approximately 10 m/s. The solute trapping effect is obvious. This is applied for the fine droplets with initial large undercooling. For the droplets with size larger than 5 μm, the total undercooling decreases with proceeding solidification due to recalescence, thus the solidification front velocity decrease, the planar interface will break down into cellular structure.

4.4. The effect of the particles on the microstructure of composite powders

In the present case, the TiB_2 nanoparticles are uniformly distributed in the powders. The particles are located either at the grain boundaries (Fig. 6a) or within grains (Fig. 6b). The location of the particles depends on the solidification front velocity (SFV). If the SFV reaches a critical value, the TiB_2 particles will be engulfed by the interface and located within grains. There are a variety of models or numerical solutions predicting the critical engulfment/pushing transition velocity V_{cr}, such as Stefanescu model [42], SAS model [43] and Sen et al. [44]. All of the models predict the inverse proportionality of V_{cr} to the particle size. In the present case, the SAS model is used as the following expression in view of the planar solid/liquid interface:

$$V_{cr} = \frac{\Delta\gamma_0 a_0^2}{3\eta\alpha R d} \tag{28}$$

where a_0 is the atomic diameter of the matrix, η is the liquid viscosity, α is the ratio of thermal conductivity, d is the particle/interface separation and $\Delta\gamma_0 = \gamma_{SP} - \gamma_{LP} - \gamma_{SL}$, γ_{SP}, γ_{LP} and γ_{SL} are interfacial energy between solid/particle, liquid/particle and solid/liquid respectively. The TiB_2 particles are in 25–500 nm radius according to our previous study [45] and the modeling parameters are listed in Table 2 [46]. It is required a SFV of at least 65 mm/s to engulf all of the nanoparticles. According to the predicted relationship between the undercooling and front interface velocity (Fig. 9), the minimum undercooling of the 33 K is required. The initial undercooling for most of droplets during atomization satisfies this requirement according to the above analysis. Therefore, it is predicted that the nanoparticles will be engulfed by the interface and locate within grains as Fig. 6b. However, there are many TiB_2 particles pushed into the grain boundaries (Fig. 6a) which disagree with prediction. This discrepancy is also found by Lavernia [47] on the interaction mechanisms between SiC particles and atomized aluminum alloy droplets by co-atomization. This discrepancy can be explained in two ways: (1) The SAS model is based on the assumption of the planar interface. This assumption is applicable when the particles are greatly finer than the curvature of the solid/liquid interface especially in the case of castings. However, the V_{cr} will tend to be infinite when the particles size is comparable with the curvature of the interface especially in the case of atomization. Thus these particles will be pushed into grain boundaries; (2) the relationship between undercooling and droplet size is based on the absence of potent catalytic sites. In the present work, the

Table 2
Parameters used for calculation of critical velocity.

Parameters	Units	Values
$\Delta\gamma_0$	J m^{-2}	0.4
a_0	m	2.55×10^{-10}
η	N S m^{-2}	0.001
α	–	0.374
d	m	1.43×10^{-8}

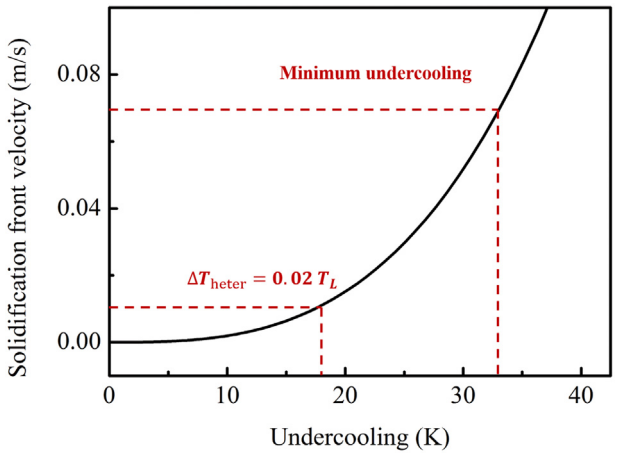

Fig. 10. The undercooling and solidification front velocity required for engulfment.

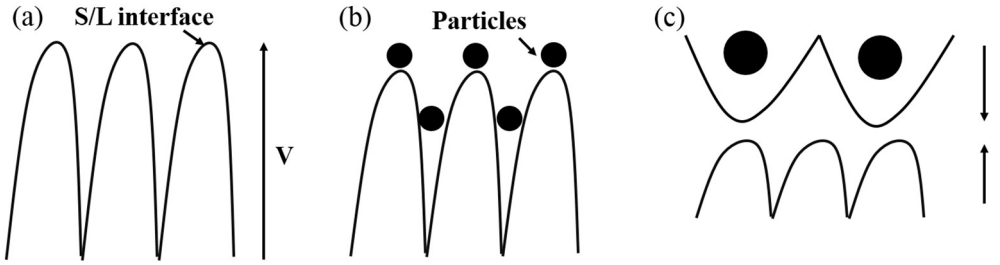

Fig. 11. (a) The illustration of the dendrite/cellular growth in the alloy droplet; (b) the illustration of the interaction of particles with the solid/liquid interface; (c) the schematic overview of the microstructure development for multiple nucleation.

solid may preferentially nucleate at the surface of TiB_2 particles. As it was mentioned above, the nucleation cannot be suppressed until large undercooling due to heterogeneous nucleation. The nucleation can even occur at the small undercooling of $0.02T_L$ (Fig. 10) and thus interface front velocity cannot satisfy the demand of engulfing the nanoparticles.

Compared to the complex microstructures of the alloy powders, the microstructure of the composite powders is nearly equiaxed. Generally, the effect of particles on the microstructure of the powders can be summarized as follows:

(1) The temperature gradient in front of the solid/liquid interface is disturbed by the particles. In the directional solidification process of alloys, the columnar grains develop along the most heat extraction direction under a large thermal undercooling [48,49], as illustrated in Fig. 11a. During the process of solidification of composite droplets, the interface shape and thermal field are influenced by the thermal conductivity ratio between the front TiB_2 particles to *Al* [50–52] as shown in Fig. 11b. In the present case, the thermal conductivity of TiB_2 is lower than that of Al. The dissipation of latent heat from the solid/liquid interface is prevented by the densely packed particles in front of the interface, which leads to temperature increment at the interface. Therefore, the interface instability would be suppressed.

(2) The particles engulfed by the solid/liquid interface can act as heterogeneous nucleation sites. There are many studies investigating the heterogeneous nucleation of inoculated aluminum alloys with *Al*-Ti-B master alloy [13–15]. With the addition of *Al*-Ti-B master alloy, the spacing of columnar/dendrite grains gradually refined. With the further addition of master alloy, a fully equiaxed grain structure was eventually formed. The heterogeneous nucleation mechanisms for TiB_2 particles have been investigated both by experiments and molecular dynamics modeling [15,53]. It was indicated that the aluminum crystals were preferentially nucleated on the {0001} surfaces of the TiB_2 particles confirmed by TEM observation. Although the aluminum crystals are preferentially nucleated at larger TiB_2 particles rather than nanoscale TiB_2 particles, there are still a large number density of available large TiB_2 particles. Therefore, multiple nucleation events are supposed to occur in the present case. As it was mentioned above, with increasing nucleation sites, the proportion of equiaxed grains increases due to impingement of cellular microstructure. Fig. 11c shows the illustration of impingement of cellular/dendrite grains when the multiple nucleation events occur.

5. Conclusion

In this study, the Al-Zn-Mg-Cu alloy powders and TiB_2/Al-Zn-Mg-Cu composite powders were fabricated by gas atomization. The different microstructures of the alloy powders including featureless structure, cellular/dendrite and equiaxed grains were experimentally observed. In the large powders, the powders exhibit equiaxed microstructure. In the powders in the range of 7–40 μm, the powders exhibit dendrite/cellular microstructure. In the powder smaller than 1.8 μm, the solute trapping behavior occurs within the powder. And the microstructure transition occurs within the powders in the range of 1.8–7 μm. The droplet history is modeled by Newtonian thermokinetics and the nucleation temperature as a function of powder size is determined. The critical condition for solute trapping (homogeneous nucleation) is discussed based on the critical undercooling, critical cooling rate and the interface velocity which is estimated by the BCT model. The heterogeneous nucleation and non-planer solid/liquid interface influence the engulfment of the particles by the interface, which results in the location at the grain boundaries for TiB_2 particles. The disturbance of temperature field in front of the solid/liquid interface and multiple nucleation events give rise to the totally different microstructure of the alloy powders and the composite powders.

CRediT authorship contribution statement

Q. Yang: Methodology, Validation, Formal analysis, Investigation, Writing - original draft. **Y.T. Liu:** Resources, Methodology, Investigation. **J. Liu:** Investigation, Conceptualization, Writing - review & editing. **L. Wang:** Formal analysis, Investigation, Writing - review & editing. **Z. Chen:** Supervision, Project administration, Conceptualization, Writing - review & editing. **M.L. Wang:** Conceptualization, Formal analysis, Investigation. **S.Y. Zhong:** Formal analysis, Investigation, Conceptualization, Writing - review & editing. **Y. Wu:** Methodology, Investigation, Writing - review & editing. **H.W. Wang:** Methodology, Writing - review & editing.

Declaration of Competing Interest

No potential conflict of interest was reported by the authors.

Acknowledgment

This work is financially supported by the National Key Research and Development Program of China (Grant No. 2018YFB1106302); the Conseil Regional du Nord-Pas de Calais and the European Regional Development Fund (ERDF).

Appendix A. Supplementary data

Supplementary data to this article can be found online at https://doi.org/10.1016/j.matdes.2019.108045.

References

[1] Y.M. Wang, T. Voisin, J.T. Mckeown, J.C. Ye, N.P. Calta, Z. Li, Z. Zeng, Y. Zhang, W. Chen, T.T. Roehling, R.T. Ott, M.K. Santala, P.J. Dephond, M.J. Matthews, A.V. Hamza, T. Zhu, Additively manufactured hierarchical stainless steels with high strength and ductility, Nat. Mater. 17 (2018) 63–70.
[2] J.H. Martin, B.D. Yahata, J.M. Hundley, J.A. Mayer, T.A. Schaedler, T.M. Pollok, 3D printing of high-strength aluminum alloys, Nature Lett 549 (2017) 365–375.

[3] J.D. Roehling, D.R. Coughlin, J.W. Gibbs, J.K. Baldwin, J.C.E. Mertens, G.H. Campbell, A.J. Clarke, J.T. Mckeown, Rapid solidification growth mode transitions in Al-Si alloys by dynamic transmission electron microscopy, Acta Mater. 131 (2017) 22–30.
[4] S. Marola, D. Manfredi, G. Fiore, M.G. Poletti, M. Lombardi, P. Fino, L. Battezzati, A comparison of selective laser melting with bulk rapid solidification of AlSi10Mg alloy, J. Alloys Compd. 742 (2018) 271–279.
[5] M.G. Poletti, G. Fiore, F. Gili, D. Mangherini, L. Battezzati, Development of a new high entropy alloy for wear resistance: FeCoCrNiW0.3 and FeCoCrNiW0.3+5 at. % of C, Mater. Des. 115 (2017) 247–254.
[6] K.K. Ma, T. Hu, H. Yang, T. Topping, A. Yousefiani, E.J. Lavernia, J.M. Schoenung, Coupling of dislocations and precipitates: impact on the mechanical behavior of ultrafine grained Al–Zn–Mg alloys, Acta Mater. 103 (2016) 153–164.
[7] Y. Chen, N. Gao, G. Sha, S.P. Ringer, M.J. Starink, Microstructural evolution, strengthening and thermal stability of an ultrafine-grained Al–Cu–Mg alloy, Acta Mater. 109 (2016) 202–212.
[8] X.P. Li, G. Ji, Z. Chen, A. Addad, Y. Wu, H.W. Wang, J. Vieugeis, J. Van Humbeeck, J.P. Kruth, Selective laser melting of nano-TiB2 decorated AlSi10Mg alloy with high fracture strength and ductility, Acta Mater. 129 (2017) 183–193.
[9] E.J. Lavernia, J.D. Ayers, T.S. Srivatstan, Rapid solidification processing with specific application to aluminum alloys, Int. Mater. Rev. 37 (1992) 1–44.
[10] G.J. Merchant, S.H. Davis, Kinetic effects in directional solidification, Appl. Mech. Rev. 43 (1990) 76–78.
[11] R. Trivedi, F. Jin, I.E. Anderson, Dynamical evolution of microstructure in finely atomized droplets of Al-Si alloys, Acta Mater. 51 (2003) 289–300.
[12] E.S. Lee, S. Ahn, Solidification progress and heat transfer analysis of gas-atomized alloy droplets during spray forming, Acta Metall. Mater. 42 (1994) 3231–3243.
[13] Y.J. Xu, D. Casari, Q. Du, R.H. Mathiesen, L. Arnberg, Y.J. Li, Heterogeneous nucleation and grain growth of inoculated aluminum alloys: an integrated study by in-situ X-radiography and numerical modelling, Acta Mater. 140 (2017) 224–239.
[14] Z.N. Chen, H.J. Kang, G.H. Fan, J.H. Li, Y.P. Lu, J.C. Jie, Y.B. Zhang, T.J. Li, X.G. Jian, T.M. Wang, Grain refinement of hypoeutectic Al-Si alloys with B, Acta Mater. 120 (2016) 168–178.
[15] Z. Fan, Y. Wang, Y. Zhang, T. Qin, X.R. Zhou, G.E. Thompson, T. Pennycook, T. Hashimoto, Grain refining mechanism in the Al/Al–Ti–B system, Acta Mater. 84 (2015) 292–304.
[16] Q. Zhang, R.H. Rangel, E.J. Lavernia, Nucleation phenomena during co-injection of ceramic particulates into atomized metal droplets, Acta Mater. 44 (1996) 3693–3703.
[17] R.J. Feller, C. Beckermann, Modeling of solidification of metal-matrix particulate composites with convection, Metall. Mater. Trans. B Process Metall. Mater. Process. Sci. 28 (1997) 1165–1183.
[18] Z. Chen, J. Li, A. Borbely, G. Ji, S.Y. Zhong, Y. Wu, M.L. Wang, H.W. Wang, The effects of nanosized particles on microstructural evolution of an in-situ TiB2/6063Al composite produced by friction stir processing, Mater. Des. 88 (2015) 999–1007.
[19] K. Kusy, M. Behulova, P. Grgac, Influence of the thermal history of a particle during atomization on the morphology of carbides in a hypereutectic iron based alloy, J. Alloys Compd. 536 (2012) 541–545.
[20] Q.Q. Lu, J.R. Fontaine, G. Aubertin, Numerical study of the solid particle motion in grid-generated turbulent flows, Int. J. Heat Mass Transf. 36 (1993) 79–87.
[21] Y.H. Su, C.Y.A. Tsao, Modeling of solidification of molten metal droplet during atomization, Metall. Mater. Trans. B Process Metall. Mater. Process. Sci. 28 (1997) 1249–1255.
[22] G. Shuo, Solidification Behavior of Spray Deposited Al-Zn-Mg-Cu Alloys and their Microstructural Evolution during Thermal Processing, PhD's degree dissertation Harbin Institute of Technology 2011 (in Chinese).
[23] C. Gonzalez, O. Alvarez, J. Genesca, J.A. Juarez-Islas, Solidification of chill-cast Al-Zn-Mg alloys to be used as sacrificial anodes, Metall. Mater. Trans. A 34 (12) (2003) 2991–2997.
[24] W.J. Boettinger, L. Bendersky, J.G. Early, An analysis of the microstructure of rapidly solidified Al-8 wt pct Fe powder, Metall. Trans. A. 17 (1986) 781–790.
[25] C.G. Levi, R. Mehrabian, Heat flow during rapid solidification of undercooled metal droplets, Metall. Trans. A. 13 (1982) 221–234.
[26] J.E. Rodriguez, C. Kreischer, T. Volkmann, D.M. Matson, Solidification velocity of undercooled Fe-Co alloys, Acta Mater. 122 (2017) 431–437.
[27] W.B. Guan, Y.L. Gao, Q.J. Zhai, K.D. Xu, Effect of droplet size on nucleation undercooling of molten metals, J. Mater. Sci. 39 (2004) 4633–4635.
[28] J.P. Hirth, Nucleation, undercooling and homogeneous structures in rapidly solidified powders, Metall. Trans. A. 9 (1978) 401–404.
[29] S. Hariprasad, S.M.L. Sastry, K.L. Jerina, Undercooling and supersaturation of alloying elements in rapidly solidified Al-8.5% Fe-1.2% V-1.7% Si alloy, J. Mater. Sci. 31 (1996) 921–925.
[30] R.F. Cochrane, P.V. Evans, A.L. Greer, Containerless solidification of alloys in a drop-tube, Mater. Sci. Eng. 98 (1988) 99–103.
[31] M. Gupta, F.A. Mohamed, E.J. Lavernia, Solidification characteristics of atomized Al-Ti powders, Scr. Metall. 26 (1992) 697–702.
[32] Y. Abe, K. Miyazawa, M. Nakamura, Solidification phenomena in formation process of rapidly solidified metallic wire, Mater. Sci. Eng. A 98 (1988) 351–355.
[33] S.G. Kim, S.H. Shin, T. Suzuki, T. Umeda, Numerical analysis of the rapid solidification of gas-atomized Al-8 Wt Pct Fe droplets, Metall. Mater. Trans. A 25 (1994) 2815–2826.
[34] J. Lipton, W. Kurz, R. Trivedi, Rapid dendrite growth in undercooled alloys, Acta Metall. 35 (1987) 9577–9964.
[35] W. Kurz, B. Giovanola, R. Trivedi, Theory of microstructural development during rapid solidification, Acta Metall. 34 (1986) 823–830.
[36] W.J. Boettinger, S.R. Coriell, A.L. Greer, A. Karma, W. Kurz, M. Rappaz, R. Trivedi, Solidification microstructures: recent developments, future directions, Acta Mater. 48 (2000) 43–70.
[37] V. Villaret, F. Deschaux-Beaume, C. Bordreuil, A solidification model for the columnar to equiaxed transition in welding of a Cr-Mo ferritic stainless steel with Ti as inoculant, J. Mater. Process. Technol. 233 (2016) 115–124.
[38] D.W. Heard, J. Boselli, R. Rioja, E.A. Marquis, R. Gauvin, M. Brochu, Interfacial morphology development and solute trapping behavior during rapid solidification of an Al–Li–Cu alloy, Acta Mater. 61 (2013) 1571–1580.
[39] D.W. Heard, R. Gauvin, M. Brochu, Non-equilibrium solute partitioning in a laser re-melted Al–Li–Cu alloy, Acta Mater. 61 (2013) 7432–7436.
[40] W.W. Mullins, R.F. Sekerka, Stability of a planar interface during solidification of a dilute binary alloy, J. Appl. Phys. 35 (1964) 444–451.
[41] R. Trived, W. Kurz, Morphological stability of a planar interface under rapid solidification conditions, Acta Metall. 34 (1986) 1663–1670.
[42] D.M. Stefanescu, B.K. Dhindaw, S.A. Kacar, A. Moitra, Behavior of ceramic particles at the solid-liquid metal interface in metal matrix composites, Metall. Trans. A. 19 (1988) 2847–2855.
[43] D. Shangguan, S. Ahuja, D.M. Stefanescu, An analytical model for the interaction between an insoluble particle and an advancing solid/liquid interface, Metall. Trans. A. 23 (1992) 669–680.
[44] S. Sen, F. Juretzko, D.M. Stefanescu, B.K. Dhindaw, P.A. Curreri, In situ observations of interaction between particulate agglomerates and an advancing planar solid/liquid interface: microgravity experiments, J. Cryst. Growth 204 (1999) 238–242.
[45] Y. Tang, Z. Chen, A. Borbely, G. Ji, S.Y. Zhong, D. Schryvers, V. Ji, H.W. Wang, Quantitative study of particle size distribution in an in-situ grown Al–TiB_2 composite by synchrotron X-ray diffraction and electron microscopy, Mater. Charact. 102 (2015) 131–136.
[46] Y.M. Youssef, R.J. Dashwood, P.D. Lee, Effect of clustering on particle pushing and solidification behaviour in TiB_2 reinforced aluminum PMMCs, Compos. Part A 36 (2005) 747–763.
[47] Y. Wu, E.J. Lavernia, Interaction mechanisms between ceramic particles and atomized metallic droplets, Metall. Trans. A. 23 (1992) 2923–2937.
[48] L.A. Khalil, G.S.A. Jaoude, G. Reinhart, C. Pickmann, G. Zimmermann, H.N. Thi, Influence of gravity level on Columnar-to-Equiaxed Transition during directional solidification of Al – 20 wt.% Cu alloys, 110 (2016) 44–52.
[49] L. Abou-Khalil, G. Salloum-Abou-Jaoude, G. Reinhart, C. Pickmann, G. Zimmermann, H. Nguyen-Thi, Influence of gravity level on Columnar-to-Equiaxed Transition during directional solidification of Al–20 wt.% Cu alloys, Acta Mater. 110 (2016) 44–52.
[50] J.W. Garvin, H.S. Udaykumar, Particle–solidification front dynamics using a fully coupled approach, part I: methodology, J. Cryst. Growth 252 (2003) 451–466.
[51] S.S.L. Peppin, J.S. Wettlaufer, Experimental verification of morphological instability in freezing aqueous colloidal suspensions, Phys. Rev. Lett. 100 (2008) 1–4.
[52] L. Hadji, Morphological instability induced by the interaction of a particle with a solid-liquid interface, Eur. Phys. J. B. 37 (2004) 85–89.
[53] B.S. Murty, S.A. Kori, M. Chakraborty, Grain refinement of aluminum and its alloys by heterogeneous nucleation and alloying, Int. Mater. Rev. 47 (2002) 3–27.